Supporting Information

Accessing polyanionic redox in high-voltage Li-rich thiophosphate-type materials

Pezhman Zarabadi-Poor[1,2,7], Jungwoo Lim[3,4,7, §], Xuefei Wang[3,7, §], Joshua D. Bocarsly[6,7], Matthew A. Wright[3,4,7], Andrés Acin-Lalanza[3,4,7], Luke M. Daniels[3,7], Ioanna M. Pateli[3,4,5,7] Alex R. Neale[3,4,7], Ruiyong Chen[3,7], John B. Claridge[3,7], Clare P. Grey[6,7], Benjamin J. Morgan[2,7], Laurence J. Hardwick [3,4,7,*], Matthew J. Rosseinsky[3,7*], M. Saiful Islam[1,2,7,*]

[1]Departments of Materials, University of Oxford, Oxford, OX1 3PH, United Kingdom
[2]Department of Chemistry, University of Bath, Bath BA2 7AY, United Kingdom
[3]Department of Chemistry, University of Liverpool, Liverpool, L69 7ZD, United Kingdom
[4]Stephenson Institute for Renewable Energy, University of Liverpool, Peach Street, Liverpool L69 7ZF, United Kingdom
[5]School of Chemistry, University of St Andrews, St Andrews, Fife KY16 9ST, United Kingdom
[6]Yusuf Hamied Department of Chemistry, University of Cambridge, Cambridge CB2 1EW, United Kingdom
[7]The Faraday Institution, Harwell Campus, Didcot OX11 0RA, United Kingdom
§ These authors contributed equally to this work

Corresponding authors: saiful.islam@materials.ox.ac.uk, m.j.rosseinsky@liverpool.ac.uk, hardwick@liverpool.ac.uk

Supplementary Note 1: Structural characterisation

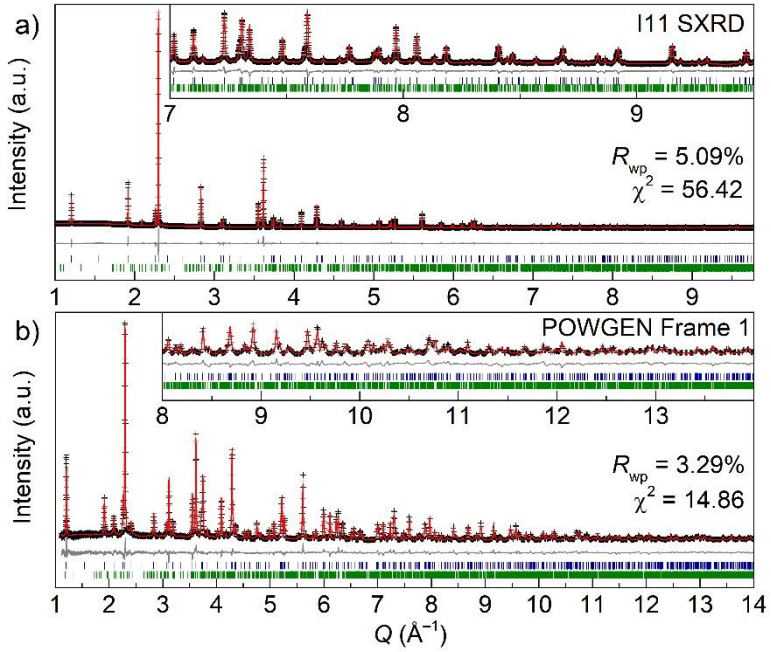

Supplementary Figure 1. Rietveld refinement against a) SXRD data (I11, Diamond Light Source) and b) NPD data (POWGEN Frame 1, SNS) of $Li_2FeP_2S_6$ measured at 298 K with I_{obs} (black crosses), I_{calc} (red line), I_{obs}-I_{calc} (grey line), and Bragg reflections (blue tick marks for $Li_2FeP_2S_6$, green tick marks for a minor Fe_7S_8 impurity phase which amounts to 3.4(4)%).

Supplementary Table 1. Structural parameters for $Li_2FeP_2S_6$ from a combined Rietveld refinement against synchrotron and neutron powder diffraction data.

Refinement parameters		
Formula	$Li_2FeP_2S_6$	
Temperature (K)	300	
Pressure	Atmospheric	
Source	Synchrotron X-ray (I11)	Neutron (POWGEN) Frame 1
Wavelength (Å)	0.826899	0.8
d spacing range (Å)	0.57-7.29	0.35-5.62
2θ range (°)/TOF range (μsec)	6.5-92.1	8000-127000
No. of reflections	443	1747
No. of refined parameters	79	
R_p	3.15	3.45
R_{wp}	5.09	3.29
R_{exp}	0.68	0.86
X^2	56.42	14.86

Structure parameters for $Li_2FeP_2S_6$

Space group	**Z**	**Density (g cm^{-3})**	**Formula weight (g mol^{-1})**
$P\bar{3}1m$	1	2.60642(1)	323.23

***a* (Å)**	***c* (Å)**	***α* (°)**	***γ* (°)**	**Volume (Å^3)**
6.018578(9)	6.565233(17)	90	120	205.953(1)

Atom	**Site**	***x***	***y***	***z***	**Occupancy**	**U_{iso} (Å^2)**
Li1	2*d*	0.3333	0.6667	0.5	0.5083(9)	0.0145(2)
Fe1	2*d*	0.3333	0.6667	0.5	0.4917(9)	0.0145(2)
Li2	2*c*	0.3333	0.6667	0	0.487(9)	0.0422(3)
P1	2*e*	0	0	0.33147(13)	1	0.00890(13)
S1	6*k*	0.32702(8)	0	0.25572(11)	1	0.00933(7)

Supplementary Table 2. Structural parameters for $Li_2Fe_{0.8}Mn_{0.2}P_2S_6$ from a combined Rietveld refinement against synchrotron and neutron powder diffraction data.

Refinement parameters		
Formula	$Li_2Fe_{0.8}Mn_{0.2}P_2S_6$	
Temperature (K)	300	
Pressure	Atmospheric	
Source	Synchrotron X-ray (I11)	Neutron (POWGEN) Frame 1
Wavelength (Å)	0.826899	0.8
d spacing range (Å)	0.57-7.29	0.40-5.62
2θ range (°)/TOF range (μsec)	6.5-92.1	9180-127000
No. of reflections	445	1180
No. of refined parameters	76	
R_p	4.07	4.53
R_{wp}	6.77	3.78
R_{exp}	0.96	1.05
X^2	49.43	13.02

Structure parameters for $Li_2Fe_{0.8}Mn_{0.2}P_2S_6$

Space group	**Z**	**Density (g cm^{-3})**	**Formula weight (g mol^{-1})**
$P\bar{3}1m$	1	2.57928(2)	321.61

***a* (Å)**	***c* (Å)**	***α* (°)**	***γ* (°)**	**Volume (Å^3)**
6.03222(2)	6.57039(3)	90	120	207.051(2)

Atom	**Site**	***x***	***y***	***z***	**Occupancy**	**U_{iso} (Å^2)**
Li1	2*d*	0.3333	0.6667	0.5	0.523(7)	0.0189(2)
Fe1	2*d*	0.3333	0.6667	0.5	0.391(7)	0.0189(2)
Mn1	2*d*	0.3333	0.6667	0.5	0.085(3)	0.0189(2)
Li2	2*c*	0.3333	0.6667	0	0.492(11)	0.0379
P1	2*e*	0	0	0.33778(18)	1	0.0291(5)
S1	6*k*	0.32906(10)	0	0.25834(11)	1	0.00668(19)

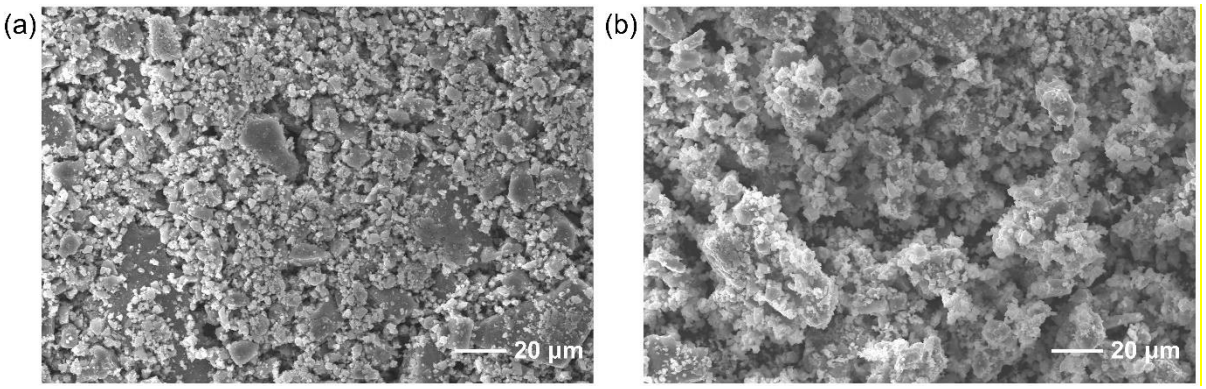

Supplementary Figure 2. SEM images of (a) $Li_2FeP_2S_6$ and (b) $Li_2Fe_{0.8}Mn_{0.2}P_2S_6$ powder samples.

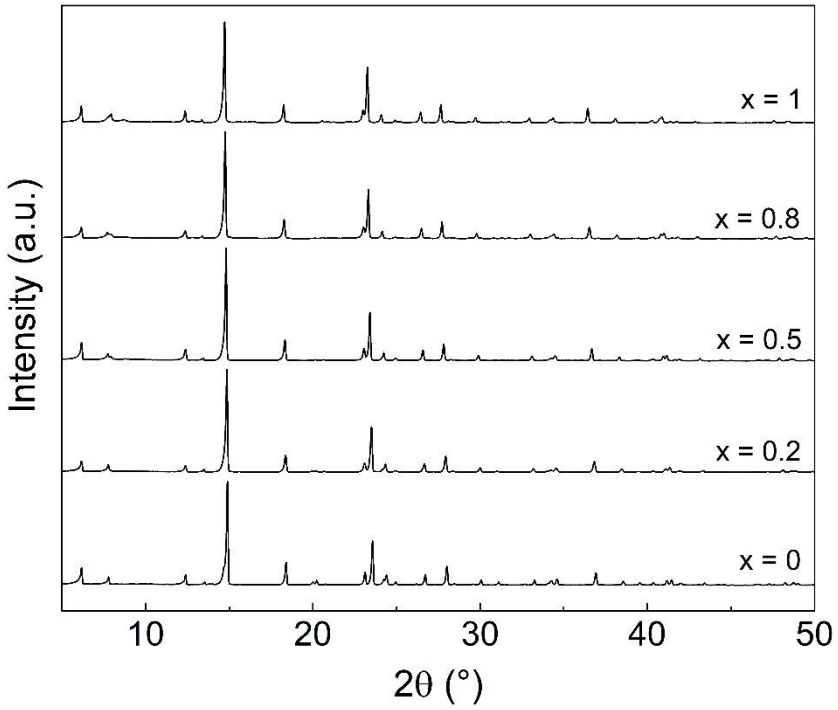

Supplementary Figure 3. Powder XRD data (Mo $K\alpha_1$, $\lambda = 0.70932$ Å), indicating the formation of phase pure compositions across the solid solution of $Li_2Fe_{1-x}Mn_xP_2S_6$.

<u>Supplementary Note 2:</u> Identification of the $Li_2Fe_2P_2S_6$ ground state structure

As noted in the main text, the presence of disordered *2c* and *2d* sites in the experimental average structure of $Li_2FeP_2S_6$ makes it necessary to identify the energetically ground state structure before any subsequent computational investigation. For this purpose, we considered a 2 × 2 × 2 supercell size that contains eight transition-metal sites. This system size enables us to investigate a wide range of compositions for transition-metal substitution at a reasonable computational cost.

We used the SUPERCELL program[1] to enumerate all symmetrically inequivalent configurations, resulting in 1,732,536 structures. This large number makes conventional computational approaches intractable. Instead, we use machine-learning techniques, specifically crystal graph convolutional neural networks (CGCNN)[2], to accelerate the computational screening. To construct a training set that captures a wide range of cation ordering, we enumerated various supercell sizes (**Supplementary Table 3**). We selected structures from the highlighted entries in **Supplementary Table 3** (1090 structures) and added 110 random structures from 2 × 2 × 2 supercell configurations, resulting in a training set of 1200 structures.

Using our in-house multistage AiiDA VASP workflows[3], we performed an initial partial relaxation (five steps) for each structure to accelerate the screening phase. Our preliminary exploration of these calculations showed a good correlation between the total energies obtained after the final static stage (E^{DFT}) and the ones after running only five ionic steps ($E^{DFT(R5)}$); hence, we used the latter energies to train our CGCNN model. To train the CGCNN model, we used most of the default hyperparameters shipped with the CGCNN code, except for the batch size and number of convolutional neural network layers. The learning curves and resulting correlation plots for training/validation/test sets are provided in **Supplementary Fig. 4**. We find that using nine convolutional neural network layers and a batch size of 16 is the best-performing combination for the current investigation. The mean absolute error (MAE) is 0.001 eV/atom.

We did not investigate the actual predictions using the trained models during the training process to avoid incorporating unconscious bias. The corresponding results for the final best model (**Supplementary Fig. 5**) show a good correlation between DFT and predicted values. Subsequently, we used the best CGCNN model to predict the energies of 1,732,536 configurations of the 2 × 2 × 2 supercell. We selected the 50 lowest-energy structures and

performed full DFT geometry relaxations. The resulting lowest energy configuration has a striped arrangement of Li/Fe sites, which was used for the remaining calculations.

Supplementary Table 3. The total number of configurations for different supercell sizes of $Li_2FeP_2S_6$ and the number of symmetry operations available to find the symmetrically unique configuration. The highlighted entries were used to construct the training set.

Supercell Size	Total number of configurations (*N*)	Unique configurations
1 × 1 × 1	4	2
1 × 1 × 2	36	10
1 × 1 × 3	400	38
1 × 2 × 1	36	12
1 × 3 × 1	400	68
2 × 1 × 1	36	12
3 × 1 × 1	400	68
1 × 2 × 2	4900	388
2 × 2 × 1	4900	140
2 × 1 × 2	4900	388
2 × 2 × 2	165636900	1732536

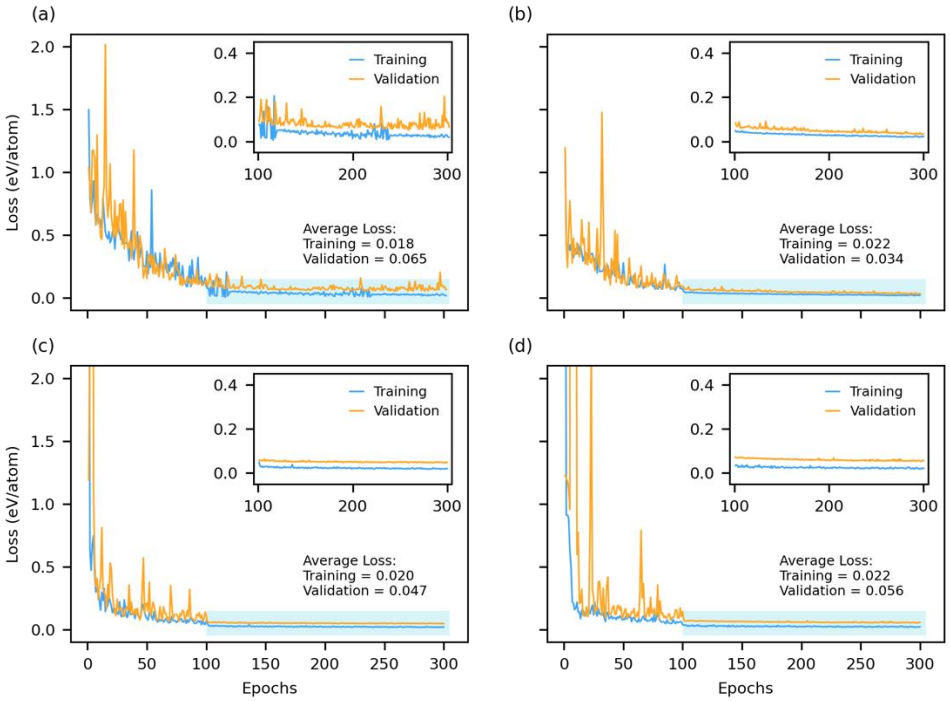

Supplementary Figure 4. Training and validation loss of CGCNN with nine convolutional neural network layers using a) 8, b) 16, c) 32, and d) 64 batch sizes (inset: magnified highlighted region for epoch range of 100-300).

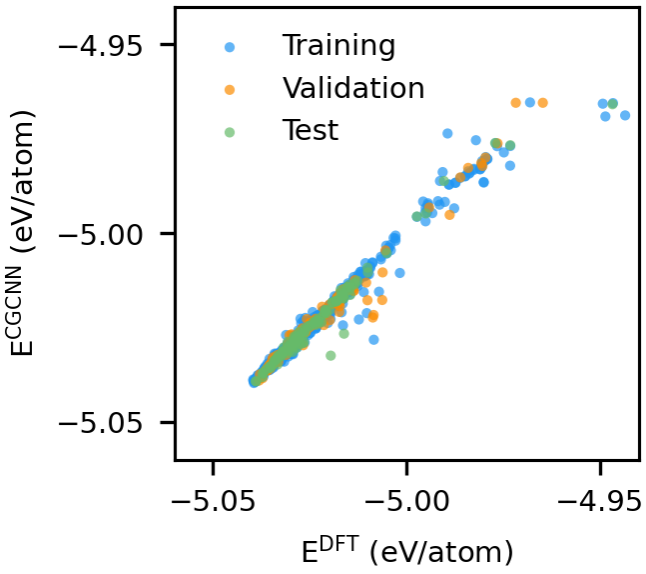

Supplementary Figure 5. Correlation of DFT energies after five steps of relaxation (E^{DFT}) with the predicted energies using the best CGCNN model for training, validation, and test set.

<u>Supplementary Note 3</u>: Neutron pair distribution function data to characterize local structure

As shown in the main manuscript **Figure 1c**, neutron pair distribution function data was used to study the local structure of $Li_2FeP_2S_6$ and $Li_2Fe_{0.8}Mn_{0.2}P_2S_6$ and evaluate the local ordering of the metals. Unlike the Bragg diffraction data, the neutron pair distribution function is especially sensitive to short-range correlations between nearby atoms, allowing us to determine whether the disordered metal sites (Li/Fe/Mn) and (Li/vacancy) in the average structure are fully randomized, or whether there is some propensity for short-range ordering.

The neutron pair distribution function $G(r)$ is derived from corrected, normalized scattering factor via a sine Fourier transform. The program PDFgetN3 was used to perform this transformation for both $Li_2FeP_2S_6$ and $Li_2Fe_{0.8}Mn_{0.2}P_2S_6$, using a Q_{max} value of 23.7 $Å^{-1}$ for $Li_2FeP_2S_6$ and 22.4 $Å^{-1}$ for $Li_2Fe_{0.8}Mn_{0.2}P_2S_6$. r_{poly} was set to 0.9 Å for both materials. These parameters were chosen to maximize resolution of the generated PDF patterns while minimizing the presence of unphysical "ripples" at low r that arise from finite counting statistics and finite Q_{max} cutoff values.

The data were fit to the average structure and to small box local structural models between a range of 1Å and 7Å in order to investigate the short-range ordering of these materials. However, at very low r values less than 1.8 Å, the PDFs are dominated by unphysical ripples due from the Fourier transform processing. Because no physical bond lengths in this system occur below ~2.0 Å (the P-S bond within the $P_2S_6^{4-}$ unit), the data between 1 and 1.8 Å was de-weighted by 100x relative to the data between 1.8 Å and 7 Å to avoid overfitting to the unphysical portion of the PDF. An $E(r)$ correction was employed in the fitting, although it was verified that fits without this correction gave similar results. For all fits, the overall composition was fixed to the nominal compositions $Li_2FeP_2S_6$ and $Li_2Fe_{0.8}Mn_{0.2}P_2S_6$. Peak shapes were handled with B_{eq} parameters on each species with a radial-dependence. Simulated annealing for the atomic positions, occupancies (within the overall composition constraints), and B_{eq} parameters was used to obtain the global best fit for each material. For $Li_2Fe_{0.8}Mn_{0.2}P_2S_6$, the transition metal position(s) were always assumed to be randomly occupied by 80% Fe and 20% Mn. In principle, it is possible that Mn and Fe (short-range) ordering occurs in this system along with the transition metal/Li we observe, however modelling this possibility in a small box was deemed to be impractical without overfitting and was not considered.

For both $Li_2FeP_2S_6$ and $Li_2Fe_{0.8}Mn_{0.2}P_2S_6$, the average structural model was found to show discrepancies to the PDF, especially in the regions associated with metal-S correlations and metal-metal correlations. We found that much better fits could be obtained by lowering the spacegroup to the subgroup *P*2/*c*, which allows for simulating local Li/vacancy and Li/(Mn,Fe) ordering (**Supplementary Figures 6-8**). Importantly, the refined locally ordered structures also show good agreement with the calculated DFT ground state, giving us increased confidence in the structural models. Furthermore, fits to structures with other patterns of metal/metal and metal/vacancy ordering were not able to provide satisfactory fits to the data.

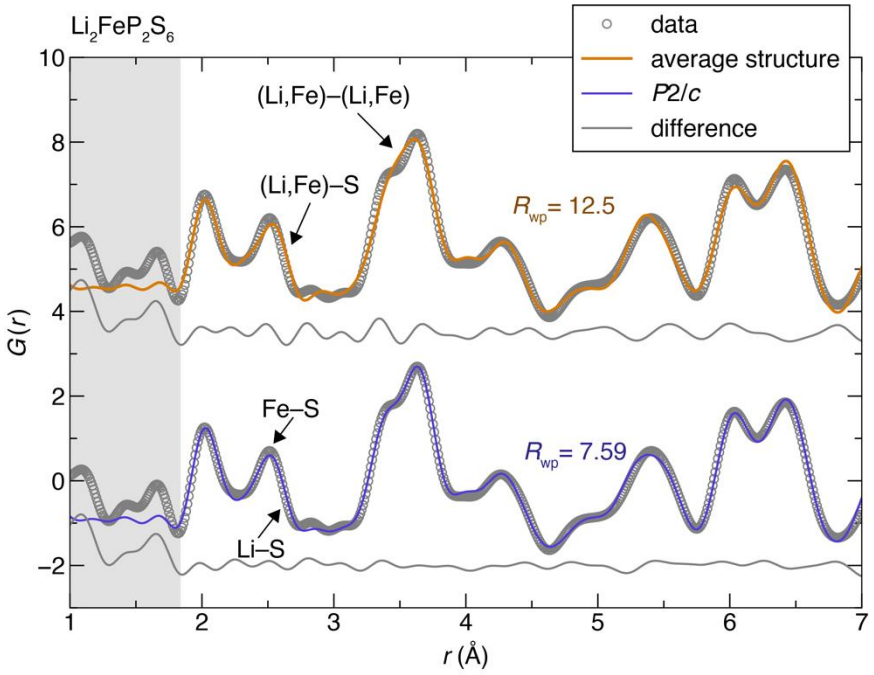

Supplementary Figure 6: Neutron pair distribution function $G(r)$ for $Li_2FeP_2S_6$, with comparison of small box fits to the average structure ($P\bar{3}1m$) and locally ordered structure (*P*2/*c*) in the range of 1Å to 7Å. The region between 1 Å and 1.8 Å contains only non-physical ripples resulting from the data processing, and therefore that region has been de-weighted in the fit to avoid overfitting to the data artifacts. The average structure fit has been vertically shifted for clarity. The arrows point to the most important regions where the average structure, fails to reproduce the structure in the PDF data, corresponding to the areas sensitive to metal ordering.

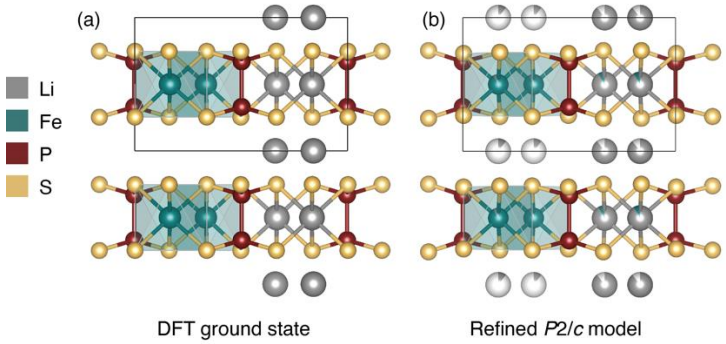

(c)

Comparison of metal-sulfur bond distances (Å) for each structure:

	Refined average structure	Refined *P2/c* short-range model	DFT ground state
Li in Li layer	2.63	2.56 - 2.70	2.57 - 2.68
Li in Fe layer	2.58	2.57 - 2.64	2.57 - 2.61
Fe	2.58	2.47 – 2.60	2.51 - 2.58

Supplementary Figure 7: Comparison of (a) the $Li_2FeP_2S_6$ ground state identified *via* CGNN computational methods and (b) the *P*2/*c* local structure refined from the short-range neutron pair distribution function data. The refined local structure is found to agree well with the computational ground state, both in terms of the occupational Li/Fe/vacancy ordering and the various metal-sulphur bond distances (c) For visualization purposes, the origin of the *P*2/*c* unit cell is shifted by (0, 0.25, 0) relative to the standard setting.

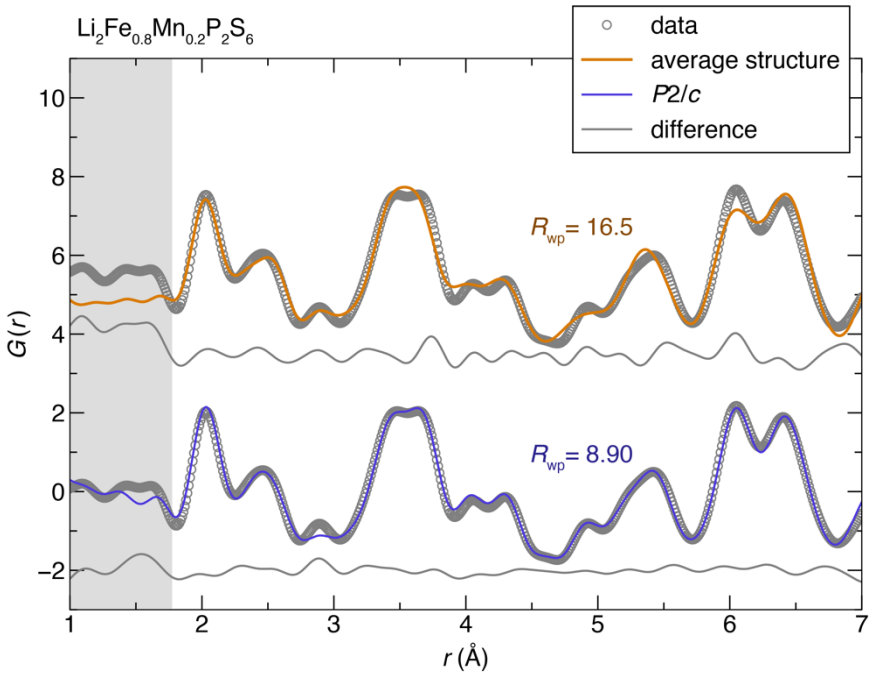

Supplementary Figure 8: Neutron pair distribution function $G(r)$ for $Li_2Mn_{0.2}Fe_{0.8}P_2S_6$, with comparison of small box fits to the average structure ($P\bar{3}1m$) and locally ordered structure (*P*2/*c*) in the range of 1Å to 7Å. The region between 1 Å and 1.8 Å contains only non-physical ripples resulting from the data processing, and therefore that region has been de-weighted in the fit to avoid overfitting to the data artifacts. The average structure fit has been vertically shifted for clarity.

Supplementary Note 4: Evaluating stability of Li_6PS_5Cl within utilised potential range

A control experiment in the all-solid-state battery with a mixture of Li_6PS_5Cl and carbon fibre (CF), without the use of any active positive electrode material (cell configuration: Li_6PS_5Cl + CF|Li_6PS_5Cl|Li) was performed at 10 mA/g at 60 °C (**Supplementary Figure 9).** There is a minor capacity contribution between 2 V and 3.5 V from the Li_6PS_5Cl solid electrolyte of less than 0.2 $mAhg^{-1}$, indicating that the vast majority of the capacity arises from the active cathode material (either $Li_2FeP_2S_6$ or $Li_2Fe_{0.8}Mn_{0.2}P_2S_6$).

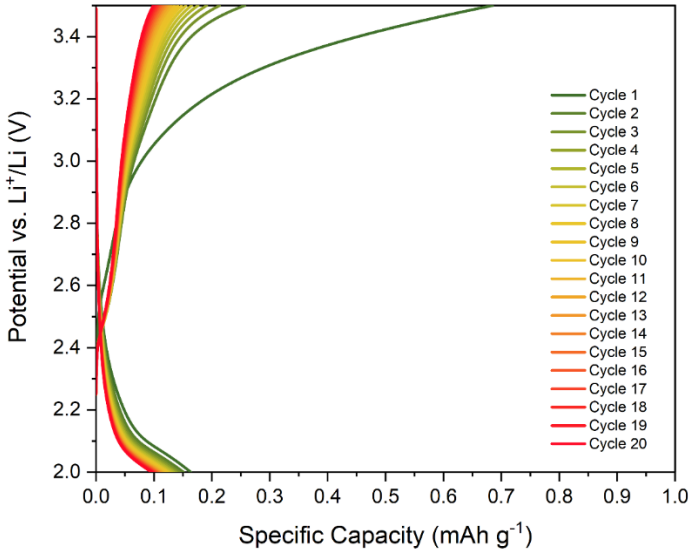

Supplementary Figure 9: Li_6PS_5Cl was cycled against Li at 10 mA/g at 60 °C in an all-solid-state configuration: Li_6PS_5Cl+CF|Li_6PS_5Cl|Li, with the positive electrode comprising of Li_6PS_5Cl and carbon fibre (83:17, w/w)

<u>Supplementary Note 5:</u> Electrochemistry of $Li_2Fe_{0.5}Mn_{0.5}P_2S_6$

Supplementary Figure 10 shows the first and second charge/discharge curves for $Li_2Fe_{0.5}Mn_{0.5}P_2S_6$. Though an initial charge of 93 mAh/g, relating to ca 1 Li^+ removal, was achieved, a discharge capacity of only ca. 28 mAh/g was realised, and second charge and discharge capacities were 27 mAh/g. Despite repeated attempts, performance improvements were not realised.

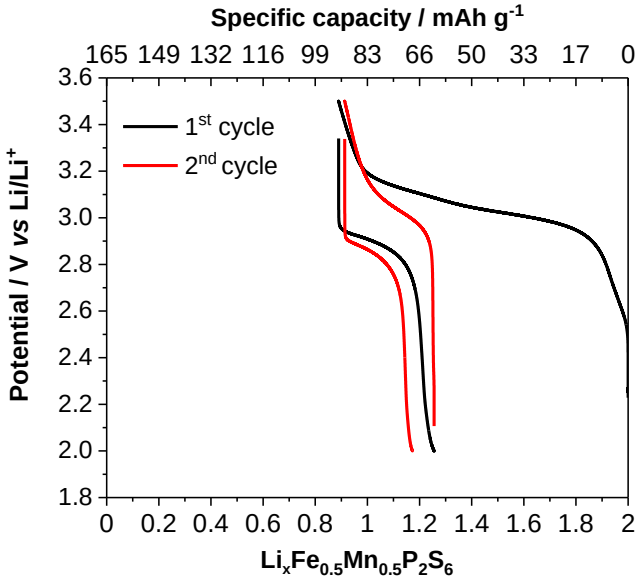

Supplementary Figure 10. 1st and 2nd discharge curve for $Li_2Fe_{0.5}Mn_{0.5}P_2S_6$ at 60 °C in and in an all-solid-state battery (ASSB) configuration with Li_6PS_5Cl as solid electrolyte vs. lithium metal.

Supplementary Note 6: Raman and ATR FT-IR

(i) Spectra for $Li_2FeP_2S_6$ and $Li_2Fe_{.8}Mn_{0.2}P_2S_6$

Raman and Attenuated Total Reflection Fourier Transform Infrared (ATR FT-IR) spectra of $Li_2FeP_2S_6$ and $Li_2Fe_{0.8}Mn_{0.2}P_2S_6$ powders were collected under an inert atmosphere (**Supplementary Fig. 11**). The $[P_2S_6]^{4-}$ framework in both materials have ethane-like motifs with D_{3d} symmetry (three-fold with an inversion mirror plane). The symmetry modes associated with the $[P_2S_6]^{4-}$ subunits are:

$$\Gamma_{vib}(P_2S_6) = \Gamma_{vib}(D_{3d}) = 3A_{1g} + 3E_g + A_{1u} + 2A_{2u} + 3E_u$$

A_{1g} and E_g are both Raman active, A_{2u} and E_u are IR active, and A_{1u} is an inactive mode. All the peaks from the pristine and ex situ samples (including the decomposition product from Li_6PS_5Cl) are summarised in **Supplementary Tables 4-5**. The Raman and IR spectra for $Li_2FeP_2S_6$ and $Li_2Fe_{.8}Mn_{0.2}P_2S_6$ show similar bands. Additional bands are observed at 380 cm^{-1} to 387 cm^{-1} and 470 cm^{-1} to 475 cm^{-1} and are assigned to P_2S_x and S_x decomposition products. **Supplementary Fig. 12** provides the extended (up to 750 cm^{-1}) ex situ Raman spectra of **Fig. 3b,** showing the absence of additional peaks, indicating no severe decomposition products exist.

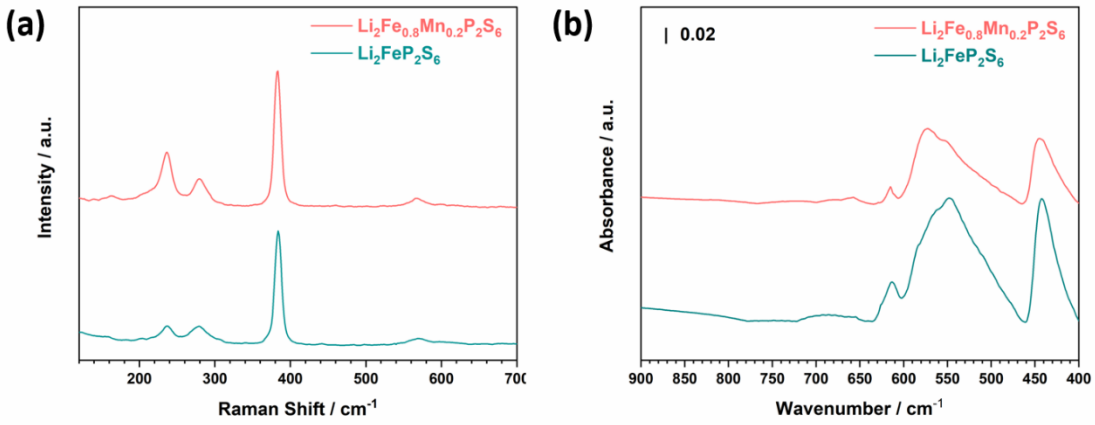

Supplementary Figure 11. Raman and IR spectra for $Li_2FeP_2S_6$ and $Li_2Fe_{.8}Mn_{0.2}P_2S_6$ powders.

Supplementary Table 4. Raman assignments for pristine and ex situ analyses of cycled electrodes of $Li_2FeP_2S_6$ and $Li_2Fe_{0.8}Mn_{0.2}P_2S_6$[4–8]

Frequency (cm^{-1})	**Assignments**
213	*v*(S-P-P) bending from P_2S_6
235	*v*(S-P-S) deformation
272	E_g from $Li_2Fe_{1-x}Mn_xP_2S_6$
380-387	A_{1g} from $Li_2Fe_{1-x}Mn_xP_2S_6$ / P_2S_x (x= 4~7) (Decomposition product from Li_6PS_5Cl)
420	$v_s(PS_4^{3-})$ from Li_6PS_5Cl
470-475	S-S-S bending from S_x (Decomposition product from Li_6PS_5Cl)
570	P-P stretching
585	P-S stretching from *v*(PS_3)

Supplementary Table 5. Infrared peak assignments for $Li_2FeP_2S_6$ and $Li_2Fe_{.8}Mn_{0.2}P_2S_6$[6,7]

Frequency (cm^{-1})	**Assignments**
442	A_{2u}
548(Fe), 574($Fe_{0.8}$)	E_u

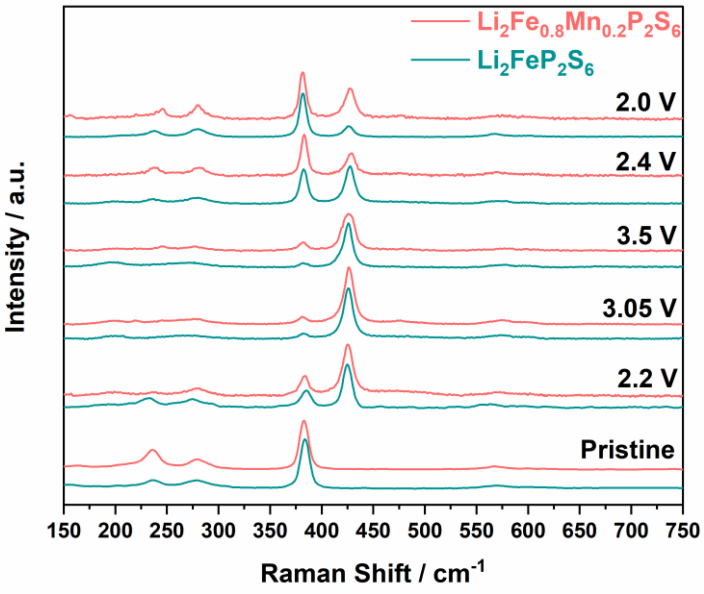

Supplementary Figure 12. Extended *ex situ* Raman spectra (**Fig. 3b**) of $Li_2FeP_2S_6$ and $Li_2Fe_{0.8}Mn_{0.2}P_2S_6$ measured at various states of charge (pristine material, 2.2 V, 3.05 V charged, 3.5 V charged, 2.4 V discharged and 2.0 V discharged), from 150 cm^{-1} to 750 cm^{-1}. No additional peaks are present between 500 cm^{-1} and 750 cm^{-1}.

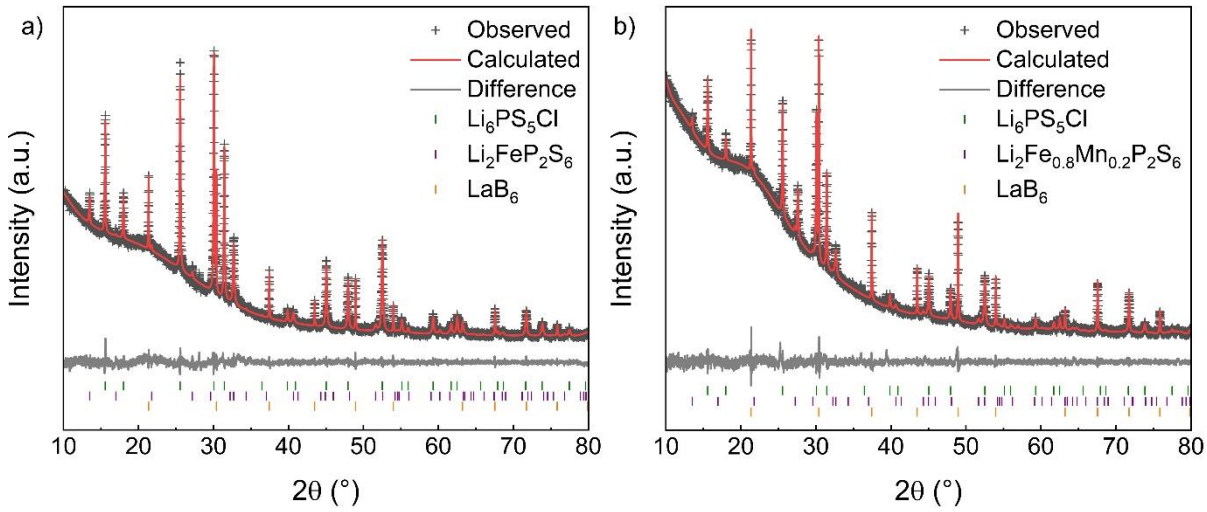

Supplementary Figure 13. Example Pawley fits against powder XRD data measured from samples of a) $Li_2FeP_2S_6$ and b) $Li_2Fe_{0.8}Mn_{0.2}P_2S_6$ cathode mixtures (a mixture of active material, Li_6PS_5Cl and carbon) after charging to 3.5 V at 60 °C. The XRD patterns show that no decomposition products are formed. LaB_6 is used as an internal standard.

(ii) Raman spectroscopy of chemically delithiated $Li_2FeP_2S_6$ and $Li_2Fe_{0.8}Mn_{0.2}P_2S_6$

Raman spectra illustrate that the chemical delithiation has not resulted in the generation of detectable side reaction products and the host compound structure remains after the chemical removal of ca. >1 lithium (**Supplementary Fig. 14**). Subtle shifts in the main $u(P_2S_6)^{4-}$ (ca. 380 cm^{-1}) peak to lower wavenumbers of 2-5 cm^{-1} are observed after delithiation (**Supplementary Table 6**). Concurrently, wavenumber shifts and sharpening of the lower bands (235, 280 cm^{-1}) of ca. 2-10 cm^{-1} are noted. These shifts are concurrent with shifts observed in both *ex situ* and *in situ* Raman measurements of electrochemically removed lithium from $Li_2FeP_2S_6$ and $Li_2Fe_{0.8}Mn_{0.2}P_2S_6$ shown in **Fig. 3b** and **Supplementary Fig. 15-17**.

***Ex situ* Raman:** Similar minor shifts (2-8 cm^{-1}) are observed in the Raman bands for the thiophosphate-type compounds that were chemical delithiated (**Supplementary Table 6).** as observed in electrochemically delithiated samples (**Supplementary Table 7)**. The main electrolyte Raman peak position for Li_6PS_5Cl remains unchanged at 426 cm^{-1} in both sets of spectra.

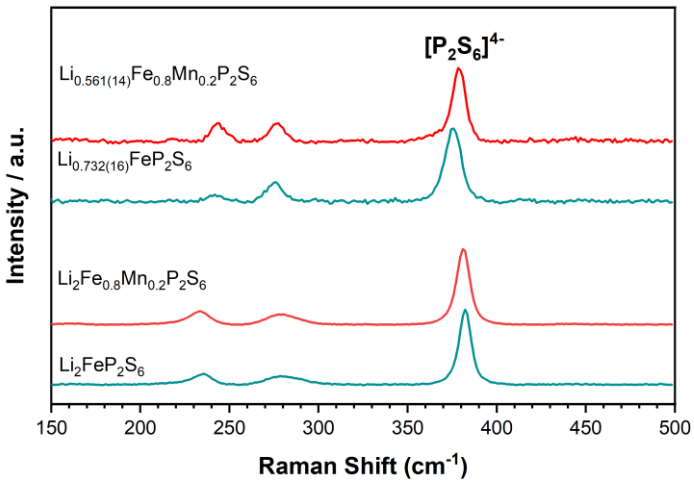

Supplementary Figure 14. Raman spectra of as-synthesised $Li_2FeP_2S_6$ and $Li_2Fe_{0.8}Mn_{0.2}P_2S_6$ and chemically delithiated $Li_{0.73}FeP_2S_6$ and $Li_{0.56}Fe_{0.8}Mn_{0.2}P_2S_6$

Supplementary Table 6. Peak positions of Raman bands of as-synthesised $Li_2FeP_2S_6$ and $Li_2Fe_{0.8}Mn_{0.2}P_2S_6$ and chemically delithiated $Li_{0.73}FeP_2S_6$ and $Li_{0.56}Fe_{0.8}Mn_{0.2}P_2S_6$

Compound	**Band position/ cm^{-1}**		
	Bending mode of P_2S_6	Bending mode of P_2S_6	$\upsilon(P_2S_6)^{4-}$
$Li_2FeP_2S_6$	235	280	382
$Li_{0.73}FeP_2S_6$	242	275	375
$Li_2Fe_{0.8}Mn_{0.2}P_2S_6$	234	279	381
$Li_{0.56}Fe_{0.8}Mn_{0.2}P_2S_6$	244	277	379

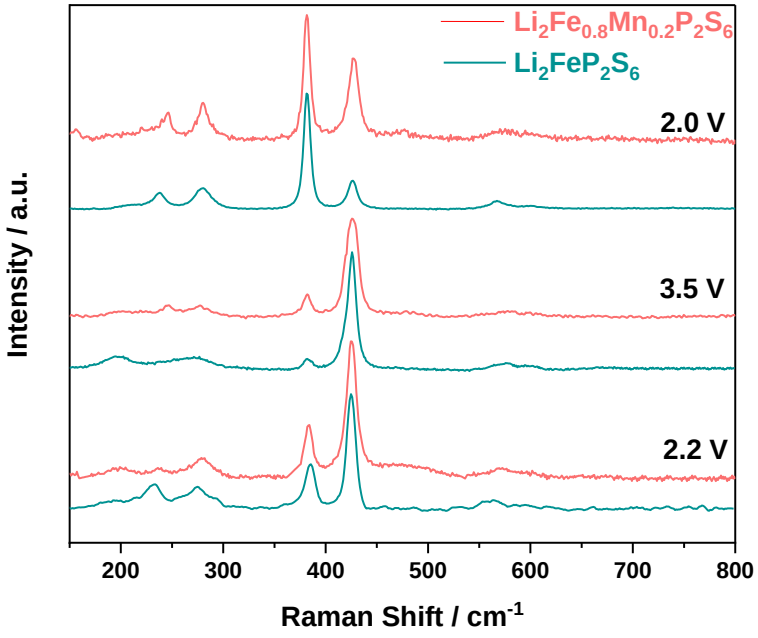

Supplementary Figure 15. Selected *ex situ* Raman spectra of analyses points 2.2 V for initial mixture, 3.5 V charged, 2.0 V discharged. No additional peaks are observed during the initial cycles.

Supplementary Table 7. Peak positions of Raman bands of electrochemically delithiated compounds. Similar shifts are observed from initial to charged states (3.5V) as measured in chemically delithiated samples.

Compound	**Band position/ cm^{-1}**		
	Bending mode of P_2S_6	Bending mode of P_2S_6	$\upsilon(P_2S_6)^{4-}$
$Li_2FeP_2S_6$:2.2 V	232	276	385
$LixFeP_2S_6$:3.5 V	-	273	383
$Li_2Fe_{0.8}Mn_{0.2}P_2S_6$:2.2 V	237	279	384
$LixFe_{0.8}Mn_{0.2}P_2S_6$:3.5 V	245	277	382

(iii) *In situ* Raman microscopy of electrochemical delithiation of $Li_2FeP_2S_6$ and $Li_2Fe_{0.8}Mn_{0.2}P_2S_6$

In situ Raman measurements were collected using a Raman microscope (Renishaw, in via Reflex coupled with an inverted Leica microscope), with a 633m nm laser as the excitation source (power < 300 μW), focussed onto the sample using a ×50 objective lens (Olympus). Spectral measurement time was 120 seconds. A solid-state in situ Raman cell was assembled by first loading the solid argyrodite electrolyte into a die (diameter: 5 mm), levelled and compressed with a cylindrical plunger (<5 MPa). The plunger was removed, and a mixture of solid-electrolyte, active material (either $Li_2FeP_2S_6$ or $Li_2Fe_{0.8}Mn_{0.2}P_2S_6$) and carbon black (55 : 40 : 5 weight ratio, that had been uniformly ground in a pestle and mortar for 30 minutes) was added to the die, on-top of the electrolyte pellet, and pressed at 360 Pa for 5 minutes. A polished lithium metal disk (diameter: 5 mm, Sigma Aldrich) was subsequently pressed onto the other side of the solid electrolyte. The whole structure was sealed in the airtight optical Raman test EL-cell (ECC-Opto-Std). In total, 25 mg of argyrodite was used as a separator layer between the positive and negative electrodes for one pellet. The total amount of the cathode composite was 3.5 mg. All these handling was performed within an argon-containing glovebox.

As with the ex situ measurements and chemically de-lithiated measurements, similar minor peak shift trends were observed, indicating the removal of lithium for the structure concurrent with the potential plateau (**Supplementary Figures 16 and 17; Supplementary Table 8**).

Supplementary Table 8. Peak positions of in situ Raman bands of electrochemically delithiated compounds at 2.5 and 3.5 V

Compound	**Band position/ cm^{-1}**		
	Bending mode of P_2S_6	Bending mode of P_2S_6	$\upsilon(P_2S_6)^{4-}$
$Li_2FeP_2S_6$:2.5 V	235	283	383
$Li_xFeP_2S_6$:3.5 V	251	270	381
$Li_2Fe_{0.8}Mn_{0.2}P_2S_6$:2.5 V	236	276	385
$Li_xFe_{0.8}Mn_{0.2}P_2S_6$: 3.5 V	243	275	381

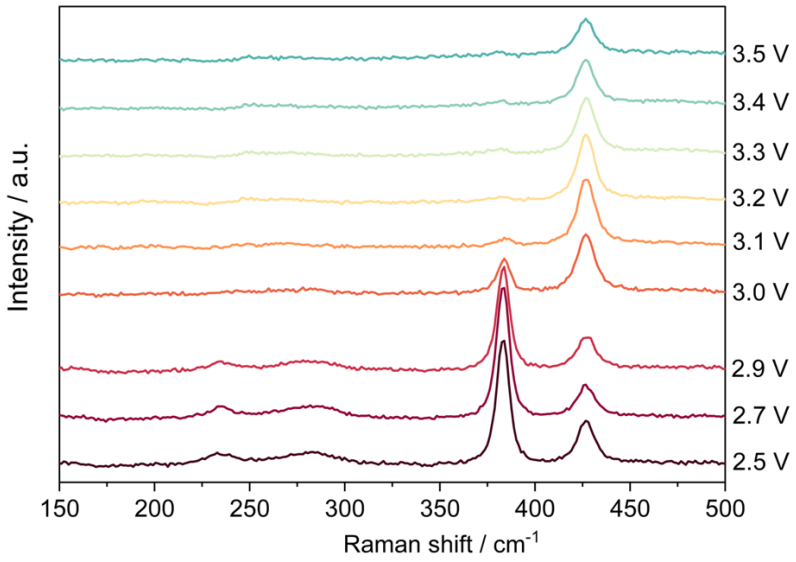

Supplementary Figure 16. *In situ* Raman microscopy of the first delithiation of $Li_2FeP_2S_6$

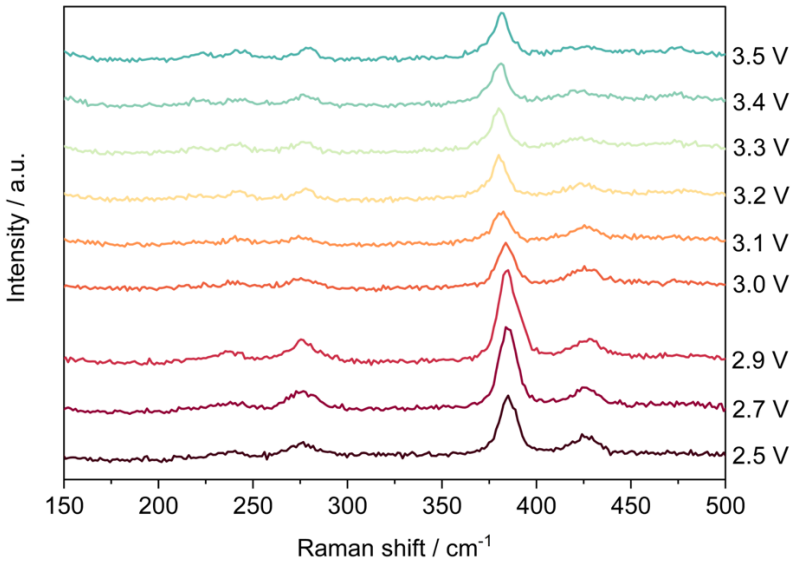

Supplementary Figure 17. *In situ* Raman microscopy of the first delithiation of $Li_2Fe_{0.8}Mn_{0.2}P_2S_6$

<u>Supplementary Note 7:</u> Hard X-ray photoelectron spectroscopy and X-ray photoelectron spectroscopy

Mn K-edge X-ray absorption near-edge spectroscopy (XANES) spectra have weak signals due to the intrinsic low content of Mn in $Li_2Fe_{0.8}Mn_{0.2}P_2S_6$, as well as dilution because of the preparation of the solid-state electrode through mixing with carbon and Li_6PS_5Cl. The redox behaviour of Mn is further examined by hard X-ray photoelectron spectroscopy (HAXPES). In addition, conventional X-ray photoelectron spectroscopy (XPS) was used to identify interfacial decomposition products. HAXPES data (**Fig. 4)** shows decomposition products at 163.46 eV from S 2*p* and 133.8 eV from P 2*p*.

The following equation demonstrates the breakdown reactions of Li_6PS_5Cl leading to P_2S_x and S_x compounds:[11,12]

$$Li_6PS_5Cl \rightarrow Li_4PS_5Cl + 2Li^+ + 2e \rightarrow Li_3PS_4 + S_x + LiCl \rightarrow P_2S_x + S_x + LiCl + 3Li^+ + 3e$$

The peak at 163.46 eV can be assigned to the 2 $p_{3/2}$ peak of S_x compound (x = 4~8, grey) and a peak at 133.8 eV to 2 $p_{3/2}$ peak of P_2S_5 (purple) which concurs with previous literature.[12,13] It should be noted that distinguishing the decomposition products, i.e. Li_3PS_4 and Li_6PS_5Cl, is challenging as both compounds consist of $[PS_4]^{3-}$ species with similar bonding characteristics. In addition, by comparing the HAXPES **(Fig. 4)** and XPS spectra **(Supplementary Fig. 18**) of $Li_2FeP_2S_6$, more significant evidence of solid electrolyte decomposition is observed between the interface of the active electrode material and the solid electrolyte.

For the deconvolution, each element shares the same full width at half maximum (FWHM) within the sample, and deconvolution is undergone with the FWHM ranging from 1.1 eV to 1.5 eV. Detailed information on the deconvolution is provided in **Supplementary Tables 9-12**. In addition, further deconvolution for 3.5 V charged $Li_2FeP_2S_6$ without polyanionic redox peaks and 3.5 V charged $Li_2Fe_{0.8}Mn_{0.2}P_2S_6$ with polyanionic redox are provided (**Supplementary Figs. 19-21**). To directly visualise the peak shape changes, normalised spectra are plotted to exemplify shape changes in $Li_2Fe_{0.8}Mn_{0.2}P_2S_6$ and $Li_2FeP_2S_6$ during charge and discharge steps (**Supplementary Fig. 22)**.

The presence of any contribution of polyanion redox peaks in $Li_2FeP_2S_6$ was examined by inclusion of the peak centres assigned to polyanionic redox obtained from the charged $Li_2Fe_{0.8}Mn_{0.2}P_2S_6$ (3.5 V) HAXPES spectra (**Supplementary Figure 21**) in the initial fit. The

inclusion of these peak centres resulted peak intensity converging to 0, highlighting no additional peak could be fitted at lower binding energy values during delithiation for $Li_2FeP_2S_6$.

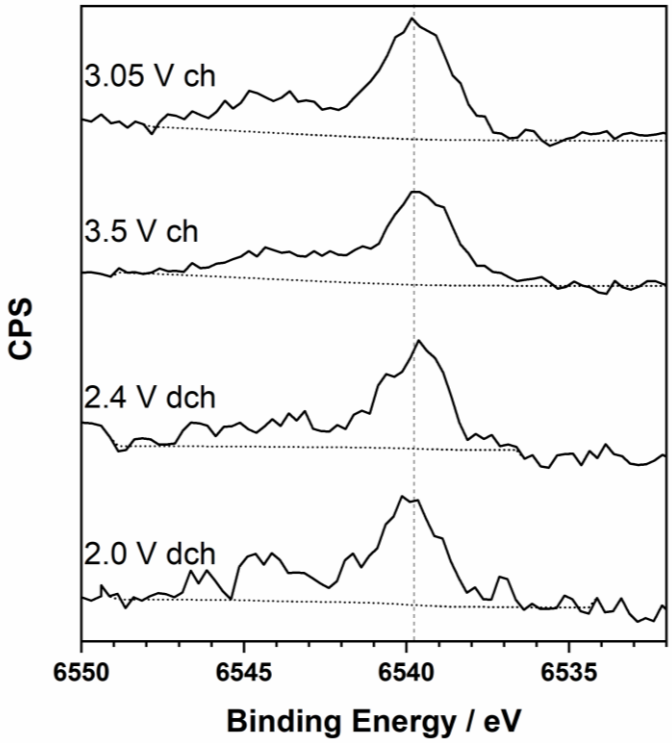

Supplementary Figure 18. Mn 1s XPS spectra for $Li_2Fe_{0.8}Mn_{0.2}P_2S_6$. Positioning was achieved via calibration to sp^3 C–C bonding from the carbon fibre standard sample. If Mn in $Li_2Fe_{0.8}Mn_{0.2}P_2S_6$ is redox-active, the binding energy will shift significantly during charge and discharge. However, the position of peaks remains unchanged within a reasonable error margin, suggesting that Mn is electrochemically inactive within $Li_2Fe_{0.8}Mn_{0.2}P_2S_6$ as observed by XANES measurements (**Fig. 3**).

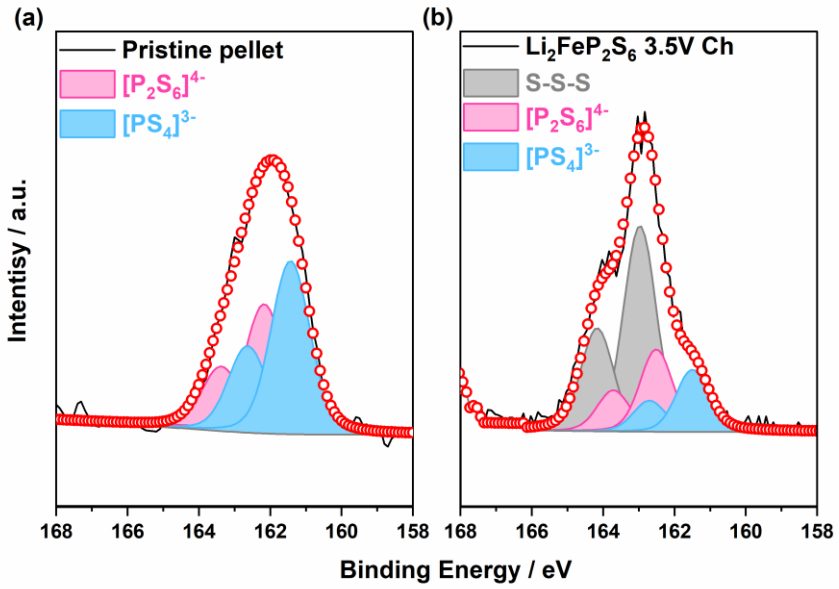

Supplementary Figure 19. XPS spectra of S 2*p* for $Li_2FeP_2S_6$. (a) pristine pellet and (b) fully charged (3.5 V) pellet. All the peaks are deconvoluted by the same full width half maximum (FWHM) and spin-orbit splitting energy (1.2 eV). Considering the bulk-dependent XRD and Raman (**Fig. 3**), peaks from the decomposition product were not found. Only minor decomposition products were found from HAXPES, which shows signals about ~100 nm from the surface (**Fig. 5**). The intensity of decomposition product within the XPS spectrum (~10 nm) (from the grey shaded peaks assigned to S_x compounds) is stronger than HAXPES, suggesting electrolyte decomposition occurs predominantly at the surface.

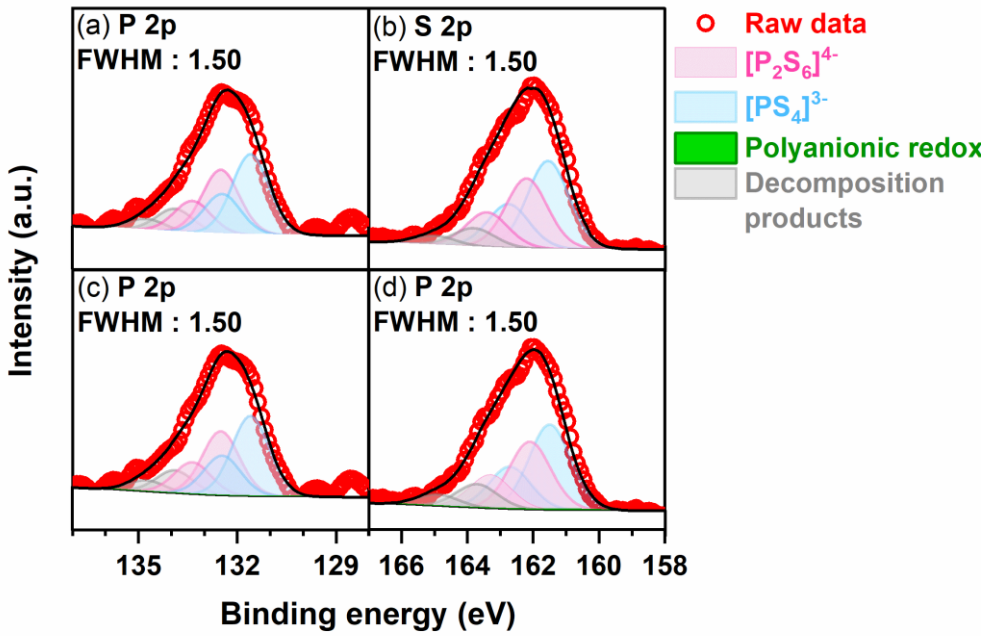

Supplementary Figure 20. HAXPES spectra and deconvolution data for 3.5 V charged $Li_2FeP_2S_6$. (a) P 2*p*, (b) S 2*p*, which have the same data as **Fig. 5**. (c) P 2*p*, (d) S 2*p*, including polyanionic redox peaks in the initial fit, whereby the peak intensity converged to 0, highlighting no additional peak could be fitted at lower binding energy values during delithiation.

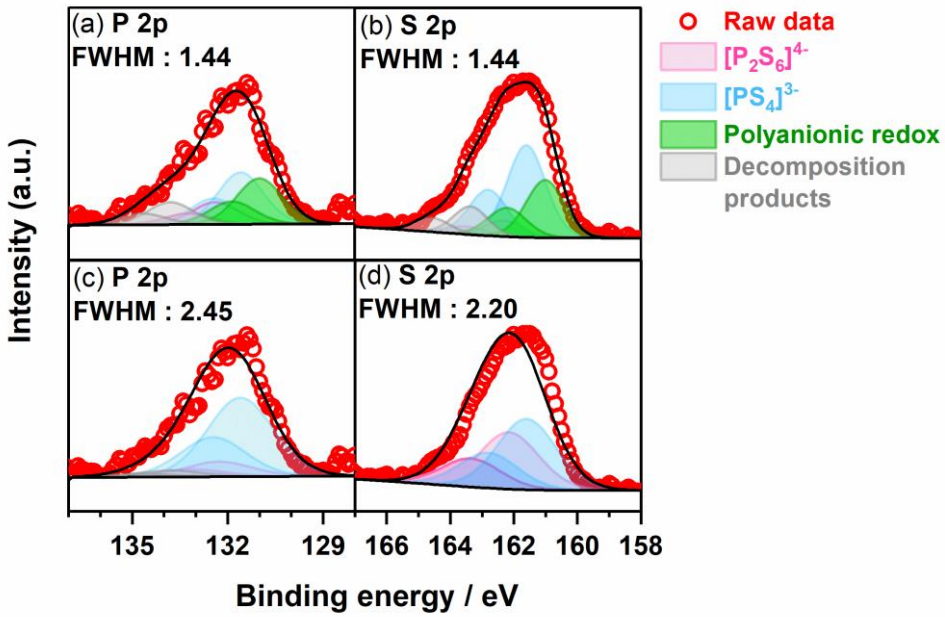

Supplementary Figure 21. HAXPES spectra and deconvolution data for 3.5 V charged $Li_2Fe_{0.8}Mn_{0.2}P_2S_6$. (a) P 2*p*, (b) S 2*p* which have same data from **Fig. 5** (c) P 2*p*, (d) S 2*p* excluding polyanionic redox peaks from the initial fit. The exclusion of polyanionic redox peaks in the initial fit causes the remaining peaks broaden significantly, increasing the peak FWHM by about 1 eV. Highlighting the inclusion of peaks assigned to polyanionic redox (green) result in an improved fit of the HAXPES spectral envelope.

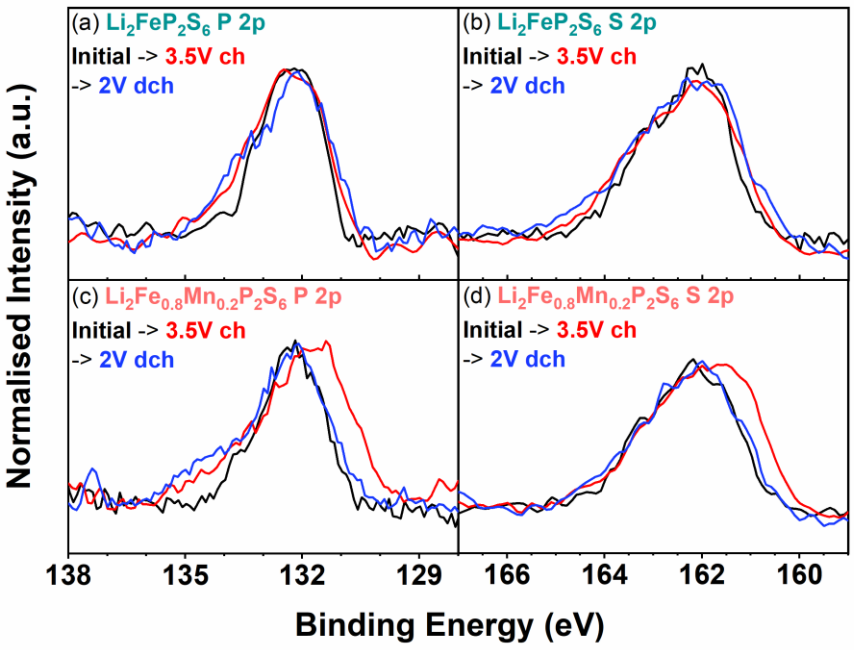

Supplementary Figure 22. Normalized P and S peaks from $Li_2FeP_2S_6$ and $Li_2Fe_{0.8}Mn_{0.2}P_2S_6$. Both compositions have minor argyrodite decomposition products above 164 eV from S 2*p* and above 134 eV from P 2*p*. The spectra from fully charged $Li_2Fe_{0.8}Mn_{0.2}P_2S_6$ shows a distinct appearance of an additional feature at lower binding energy and shape reversibly returns at 2.0 V discharged. Not all the spectra shift to lower binding energy, only the apex of the spectra shift to lower binding energy suggesting, there is additional polyanionic redox peaks exist at lower binding energy.

Supplementary Table 9. Peak deconvolution information for $Li_2FeP_2S_6$ S 2*p*. The residual standard deviation values are 0.5402 (initial), 0.788 (3.05 V charged), 1.141 (3.5 V charged), 0.765 (2.4 V discharged), 0.8338 (2.0 V discharged)

Sample	**Peak assigned**	**Spin Orbital Splitting**	**Peak location/ eV**	**FWHM/ eV**
Initial	Li_6PS_5Cl	$2p_{3/2}$	161.78	1.32
		$2p_{1/2}$	162.98	1.32
	$[P_2S_6]^{4-}$	$2p_{3/2}$	162.21	1.32
		$2p_{1/2}$	162.51	1.32
3.05 V charged	Li_6PS_5Cl	$2p_{3/2}$	161.46	1.29
		$2p_{1/2}$	162.66	1.29
	$[P_2S_6]^{4-}$	$2p_{3/2}$	162.2	1.29
		$2p_{1/2}$	163.4	1.29
	Decomposition product	$2p_{3/2}$	163.54	1.29
		$2p_{1/2}$	164.74	1.29
3.5 V charged	Li_6PS_5Cl	$2p_{3/2}$	161.55	1.50
		$2p_{1/2}$	162.75	1.50
	$[P_2S_6]^{4-}$	$2p_{3/2}$	162.2	1.50
		$2p_{1/2}$	163.4	1.50
	Decomposition product	$2p_{3/2}$	163.8	1.50
		$2p_{1/2}$	165	1.50
2.4 V discharged	Li_6PS_5Cl	$2p_{3/2}$	161.55	1.50
		$2p_{1/2}$	162.75	1.50
	$[P_2S_6]^{4-}$	$2p_{3/2}$	162.2	1.50
		$2p_{1/2}$	163.4	1.50
	Decomposition product	$2p_{3/2}$	163.8	1.50
		$2p_{1/2}$	165	1.50
2.0 V discharged	Li_6PS_5Cl	$2p_{3/2}$	161.6	1.49
		$2p_{1/2}$	162.8	1.49
	$[P_2S_6]^{4-}$	$2p_{3/2}$	162.2	1.49
		$2p_{1/2}$	163.4	1.49
	Decomposition product	$2p_{3/2}$	163.6	1.49
		$2p_{1/2}$	164.8	1.49

Supplementary Table 10. Peak deconvolution information for $Li_2FeP_2S_6$ P 2p. The residual standard deviation values are 0.49 (initial), 0.42 (3.05 V charged), 0.65 (3.5 V charged), 0.87 (2.4 V discharged), 0.69 (2.0 V discharged)

Sample	**Peak assigned**	**Spin Orbital Splitting**	**Peak location/ eV**	**FWHM/ eV**
Initial	Li_6PS_5Cl	$2p_{3/2}$	131.72	1.12
		$2p_{1/2}$	132.58	1.12
	$[P_2S_6]^{4-}$	$2p_{3/2}$	132.49	1.12
		$2p_{1/2}$	133.35	1.12
3.05 V charged	Li_6PS_5Cl	$2p_{3/2}$	131.6	1.50
		$2p_{1/2}$	132.46	1.50
	$[P_2S_6]^{4-}$	$2p_{3/2}$	132.3	1.50
		$2p_{1/2}$	133.16	1.50
	Decomposition product	$2p_{3/2}$	133.9	1.50
		$2p_{1/2}$	134.76	1.50
3.5 V charged	Li_6PS_5Cl	$2p_{3/2}$	131.6	1.34
		$2p_{1/2}$	132.46	1.34
	$[P_2S_6]^{4-}$	$2p_{3/2}$	132.5	1.34
		$2p_{1/2}$	133.6	1.34
	Decomposition product	$2p_{3/2}$	133.9	1.34
		$2p_{1/2}$	134.76	1.34
2.4 V discharged	Li_6PS_5Cl	$2p_{3/2}$	131.75	1.41
		$2p_{1/2}$	132.61	1.41
	$[P_2S_6]^{4-}$	$2p_{3/2}$	132.55	1.41
		$2p_{1/2}$	133.41	1.41
	Decomposition product	$2p_{3/2}$	133.9	1.41
		$2p_{1/2}$	134.76	1.41
2.0 V discharged	Li_6PS_5Cl	$2p_{3/2}$	131.54	1.45
		$2p_{1/2}$	132.4	1.45
	$[P_2S_6]^{4-}$	$2p_{3/2}$	132.3	1.45
		$2p_{1/2}$	133.16	1.45
	Decomposition product	$2p_{3/2}$	133.81	1.45
		$2p_{1/2}$	134.67	1.45

Supplementary Table 11. Peak deconvolution information for $Li_2Fe_{0.8}Mn_{0.2}P_2S_6$ S 2p. The residual standard deviation values are 0.62 (initial), 1.0 (3.05 V charged), 0.78 (3.5 V charged), 0.71 (2.4 V discharged), 1.3 (2.0 V discharged)

Sample	**Peak assigned**	**Spin Orbital Splitting**	**Peak location/ eV**	**FWHM/ eV**
Initial	Li_6PS_5Cl	$2p_{3/2}$	161.65	1.45
		$2p_{1/2}$	162.85	1.45
	$[P_2S_6]^{4-}$	$2p_{3/2}$	162.3	1.45
		$2p_{1/2}$	163.5	1.45
3.05 V charged	Li_6PS_5Cl	$2p_{3/2}$	161.6	1.46
		$2p_{1/2}$	162.8	1.46
	$[P_2S_6]^{4-}$	$2p_{3/2}$	162.2	1.46
		$2p_{1/2}$	163.4	1.46
	Polyanionic redox	$2p_{3/2}$	161.09	1.46
		$2p_{1/2}$	162.29	1.46
	Decomposition product	$2p_{3/2}$	163.47	1.46
		$2p_{1/2}$	164.67	1.46
3.5 V charged	Li_6PS_5Cl	$2p_{3/2}$	161.6	1.44
		$2p_{1/2}$	162.8	1.44
	$[P_2S_6]^{4-}$	$2p_{3/2}$	162.3	1.44
		$2p_{1/2}$	163.5	1.44
	Polyanionic redox	$2p_{3/2}$	161.02	1.44
		$2p_{1/2}$	161.22	1.44
	Decomposition product	$2p_{3/2}$	163.36	1.44
		$2p_{1/2}$	164.56	1.44
2.4 V discharged	Li_6PS_5Cl	$2p_{3/2}$	161.7	1.41
		$2p_{1/2}$	162.9	1.41
	$[P_2S_6]^{4-}$	$2p_{3/2}$	162.15	1.41
		$2p_{1/2}$	162.35	1.41
	Polyanionic redox	$2p_{3/2}$	161.05	1.41
		$2p_{1/2}$	162.25	1.41
	Decomposition product	$2p_{3/2}$	161.3	1.41
		$2p_{1/2}$	164.5	1.41
2.0 V discharged	Li_6PS_5Cl	$2p_{3/2}$	161.6	1.31
		$2p_{1/2}$	162.8	1.31
	$[P_2S_6]^{4-}$	$2p_{3/2}$	162.18	1.31
		$2p_{1/2}$	163.38	1.31
	Decomposition product	$2p_{3/2}$	163.45	1.31
		$2p_{1/2}$	164.65	1.31

Supplementary Table 12. Peak deconvolution information for $Li_2Fe_{0.8}Mn_{0.2}P_2S_6$ P 2p. The residual STD is 0.50 (initial), 0.69 (3.05 V charged), 0.69 (3.5 V charged), 0.85 (2.4 V discharged), 0.90 (2.0 V discharged)

Sample	**Peak assigned**	**Spin Orbital Splitting**	**Peak location/ eV**	**FWHM/ eV**
Initial	Li_6PS_5Cl	$2p_{3/2}$	131.77	1.42
		$2p_{1/2}$	132.63	1.42
	$[P_2S_6]^{4-}$	$2p_{3/2}$	132.41	1.42
		$2p_{1/2}$	133.27	1.42
3.05 V charged	Li_6PS_5Cl	$2p_{3/2}$	131.6	1.33
		$2p_{1/2}$	132.46	1.33
	$[P_2S_6]^{4-}$	$2p_{3/2}$	132.5	1.33
		$2p_{1/2}$	133.36	1.33
	Polyanionic redox	$2p_{3/2}$	130.99	1.33
		$2p_{1/2}$	131.85	1.33
	Decomposition product	$2p_{3/2}$	133.8	1.33
		$2p_{1/2}$	134.66	1.33
3.5 V charged	Li_6PS_5Cl	$2p_{3/2}$	131.6	1.45
		$2p_{1/2}$	132.46	1.45
	$[P_2S_6]^{4-}$	$2p_{3/2}$	132.4	1.45
		$2p_{1/2}$	133.26	1.45
	Polyanionic redox	$2p_{3/2}$	130.86	1.45
		$2p_{1/2}$	131.72	1.45
	Decomposition product	$2p_{3/2}$	133.8	1.45
		$2p_{1/2}$	134.66	1.45
2.4 V discharged	Li_6PS_5Cl	$2p_{3/2}$	131.6	1.30
		$2p_{1/2}$	132.46	1.30
	$[P_2S_6]^{4-}$	$2p_{3/2}$	132.5	1.30
		$2p_{1/2}$	133.6	1.30
	Polyanionic redox	$2p_{3/2}$	130.85	1.30
		$2p_{1/2}$	131.71	1.30
	Decomposition product	$2p_{3/2}$	133.8	1.30
		$2p_{1/2}$	134.66	1.30
2.0 V discharged	Li_6PS_5Cl	$2p_{3/2}$	131.6	1.41
		$2p_{1/2}$	132.46	1.41
	$[P_2S_6]^{4-}$	$2p_{3/2}$	132.4	1.41
		$2p_{1/2}$	133.26	1.41
	Decomposition product	$2p_{3/2}$	133.96	1.41
		$2p_{1/2}$	134.82	1.41

ICP-OES of chemically delithiated $Li_2FeP_2S_6$ and $Li_2Fe_{0.8}Mn_{0.2}P_2S_6$

Chemical delithiation of $Li_2FeP_2S_6$ and $Li_2Fe_{0.8}Mn_{0.2}P_2S_6$: To mitigate against the convolution of the solid electrolyte and carbon additives, $Li_2FeP_2S_6$ and $Li_2Fe_{0.8}Mn_{0.2}P_2S_6$ powers were chemically delithiated. A 3× molar excess of iodine was dissolved in 5 ml of 10/1 (v/v) hexane/DME and 50 mg of $Li_2Fe_{1-y}Mn_yP_2S_6$ (y = 0, 0.2) (1.5 moles of I_2 per Li in $Li_2Fe_{1-y}Mn_yP_2S_6$) was added before heating to 60 °C, stirring gently for 48 h. The chemically delithiated powders were characterised by ICP-OES, TEM-EDX, Raman spectroscopy, PXRD and HAXPES. ICP-OES results determined that after chemical delithiation with I_2, the Li content decreased in both $Li_2FeP_2S_6$ and $Li_2Fe_{0.8}Mn_{0.2}P_2S_6$ to $Li_{0.73(2)}FeP_2S_6$ and $Li_{0.516(12)}Fe_{0.8}Mn_{0.2}P_2S_6$ (**Supplementary Tables 13-16; Supplementary Figure 23-25).**

Supplementary Table 13. ICP-OES data for $Li_2FeP_2S_6$

Atom	MW [g/mol]	ppm				Ave conc. mmol/L	Norm. Ratio	Error/RSD
Li	6.94	18.68	24.72	22.46		3.16	2.02	0.28
Fe	55.85	87.54	87.72			1.57	1.0000	0.0015
Mn	54.94	0.11	0.12	0.12	0.18	0.00	0.00154	0.00037
P	30.97	94.61	92.45	94.33		3.03	1.930	0.024
S	32.06	270.33	269.24	265.45		8.37	5.334	0.051

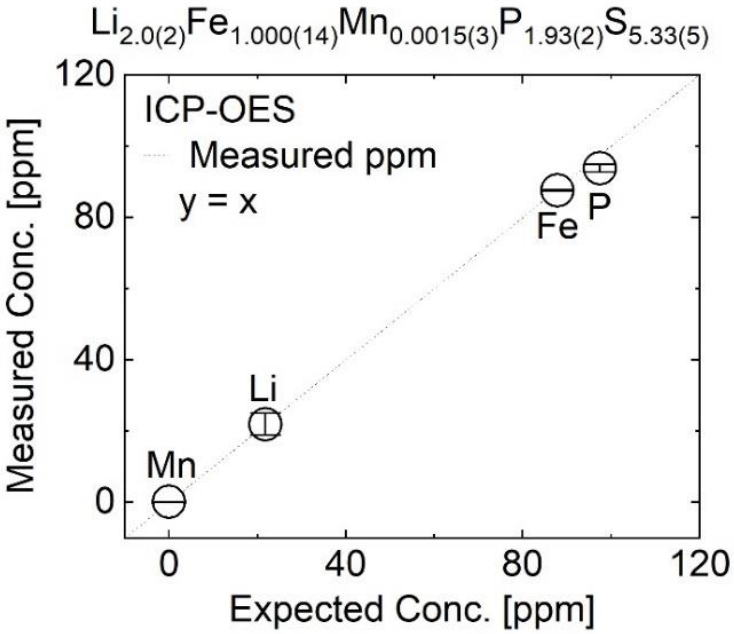

Supplementary Figure 23. ICP-OES of $Li_2FeP_2S_6$, comparing the calculated expected concentration (in ppm) versus the measured concentration.

Supplementary Table 14. ICP-OES data for $Li_2Fe_{0.8}Mn_{0.2}P_2S_6$

Atom	MW [g/mol]	ppm				Ave conc. mmol/L	Norm. Ratio	Error/RSD
Li	6.94	11.39	14.92	13.60		1.92	1.91	0.26
Fe	55.85	45.00	44.73			0.80	0.8000	0.0034
Mn	54.94	11.26	11.16	11.16	11.23	0.20	0.203053	0.00092
P	30.97	57.64	56.69	57.54		1.85	1.842	0.017
S	32.06	164.47	163.39	160.20		5.07	5.053	0.069

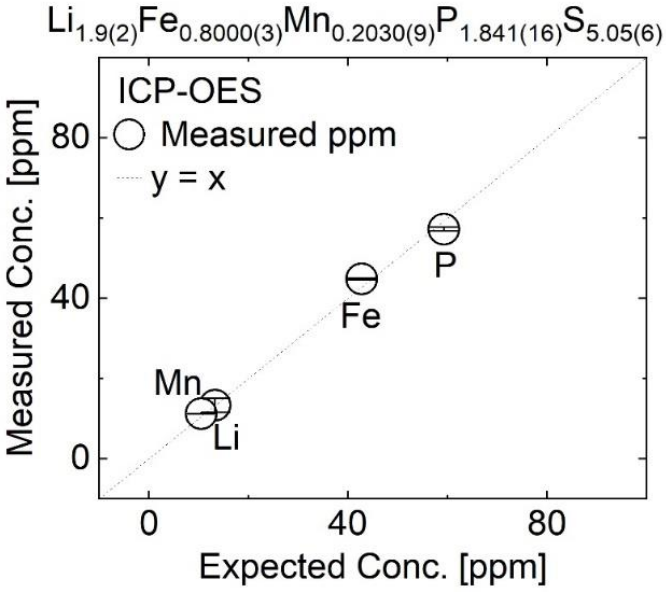

Supplementary Figure 24. ICP-OES of $Li_2Fe_{0.8}Mn_{0.2}P_2S_6$, comparing the calculated expected concentration (in ppm) versus the measured concentration.

Supplementary Table 15. ICP-OES data for $Li_{0.73(2)}FeP_2S_6$ after chemical delithiation

Atom	MW [g/mol]	ppm				Ave conc. mmol/L	Norm. Ratio	Error/RSD
Li	6.94	2.57				0.37	0.732	0.020
Fe	55.85	28.25	28.32	28.15		0.51	1.00000	0.0030
Mn	54.94	0.03	0.03	0.03	0.05	0.00	0.00126	0.00036
P	30.97	29.86	30.03			0.97	1.9118	0.0077
S	32.06	84.17	83.45			2.61	5.170	0.031

Supplementary Table 16. ICP-OES data for $Li_{0.516(12)}Fe_{0.8}Mn_{0.2}P_2S_6$ after chemical delithiation

Atom	MW [g/mol]	ppm				Ave conc. mmol/L	Norm. Ratio	Error/RSD
Li	6.94	0.81				0.12	0.516	0.012
Fe	55.85	12.62	12.66	12.64		0.23	0.8000	0.0016
Mn	54.94	3.08	3.11	3.12	3.11	0.05	0.2497	0.0013
P	30.97	12.93	12.85			0.42	1.8386	0.0081
S	32.06	36.82	36.94			1.15	5.082	0.012

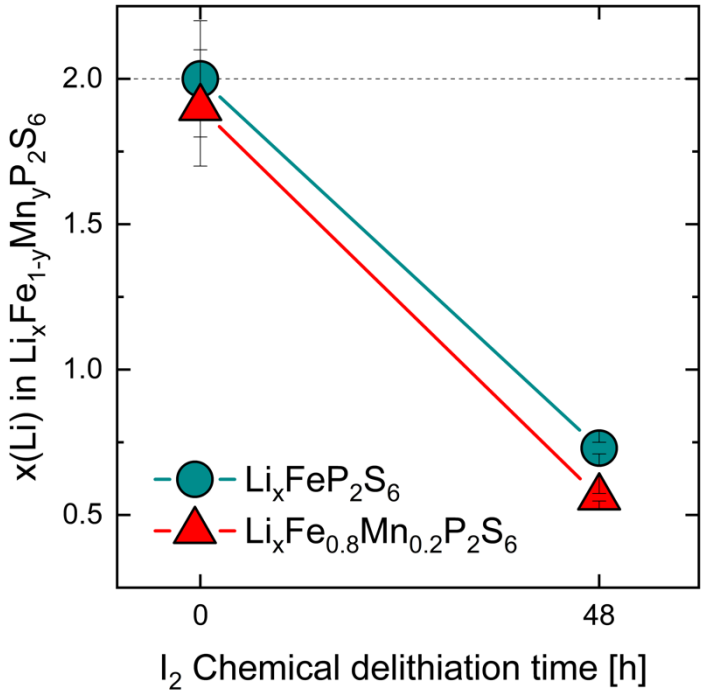

Supplementary Figure 25. Li content measured by ICP-OES of the synthesised $Li_2FeP_2S_6$ and $Li_2Fe_{0.8}Mn_{0.2}P_2S_6$ powder and chemically delithiated $Li_{0.73}FeP_2S_6$ and $Li_{0.56}Fe_{0.8}Mn_{0.2}P_2S_6$

HAXPES of chemically delithiated $Li_2FeP_2S_6$ and $Li_2Fe_{0.8}Mn_{0.2}P_2S_6$

The chemically delithiated powder samples avoid measurement of similar energy bands from the solid electrolyte (Li_6PS_5Cl) and the resultant side reaction products at the interfaces between material and solid electrolyte. As shown in **Supplementary Fig. 26** similar low energy features assigned to $[P_2S_6]^{(4-d)-}$ are shown in the delithiated $Li_{0.56}Fe_{0.8}Mn_{0.2}P_2S_6$ only (green bands). No high energy features are observed which were previously assigned to solid electrolyte decomposition products, providing further evidence supporting this assignment.

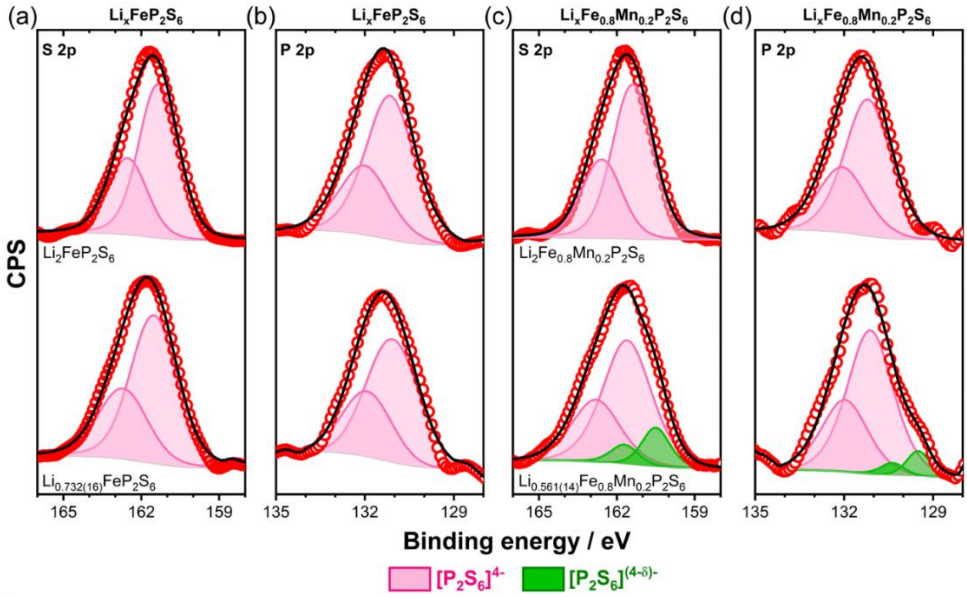

Supplementary Figure 26. HAXPES spectra and deconvolution data for S 2p and P 2p signals present in (a,b) as-synthesised $Li_2FeP_2S_6$ and $Li_2Fe_{0.8}Mn_{0.2}P_2S_6$ and (c,d) chemically delithiated $Li_{0.73}FeP_2S_6$ and $Li_{0.56}Fe_{0.8}Mn_{0.2}P_2S_6$. The red circles show raw data, while the black lines show the corresponding fitted models. Features assigned to $[P_2S_6]^{4-}$ are shown in pink, and features assigned to $[P_2S_6]^{(4-\delta)-}$ are shown in green.

Supplementary Note 8: Cluster Expansion and DFT Results

We used a cluster expansion (CE) approach to model the delithiation process by identifying the ground state structures of $Li_xFeP_2S_6$ and $Li_xFe_{0.75}Mn_{0.25}P_2S_6$ at different lithium content (x = 0.125–1.875), i.e., various states of charge. We enumerated all symmetrically distinct configurations using bsym[9], resulting in 8548 and 32896 structures for the $Li_xFeP_2S_6$ and $Li_xFe_{0.75}Mn_{0.25}P_2S_6$ systems. We used an iterative approach to construct the training set and train a CE model. For training our CE model, we used the ICET package[10] with the LASSO optimiser. We used pair and triple cut-offs of 9 Å and 4 Å, respectively, identified via searching a wide range of cut-offs and considering having low RMSE and small condition numbers. Initially, we trained a preliminary CE model using energies calculated for different configurations of fully lithiated phases. We used this CE as an initial model to predict energies for all delithiated configurations. The selected low-energy (and a few high-energy) configurations were used to construct separate training sets for $Li_xFeP_2S_6$ and $Li_xFe_{0.75}Mn_{0.25}P_2S_6$ phases, subject to full geometry and lattice relaxation. We then used these new training sets to train independent CE models for $Li_xFeP_2S_6$ and $Li_xFe_{0.75}Mn_{0.25}P_2S_6$. We repeated the energy prediction and training set updating until no more configurations were selected to be added to the training set.

Finally, we used the relative energies with respect to the current low-energy structure to compare the energies and select predicted structures without DFT results. We subsequently performed DFT calculations and added them to the training set. Afterwards, we used the final models to predict the energies of all other structures from the enumeration process. **Supplementary Fig. 27** shows the correlation plot for the DFT energy and corresponding values obtained via CE prediction. **Supplementary Fig. 28** shows the projected density of states of $Li_xFeP_2S_6$ (for x = 2 and 1); and **Supplementary Fig. 29** shows the changes in the calculated magnetic moments of Fe and Mn in $Li_xFe_{0.8}Mn_{0.2}P_2S_6$, and the changes in the calculated charges of $[P_2S_6]$ units in $Li_xFe_{0.8}Mn_{0.2}P_2S_6$ and $Li_xFeP_2S_6$.

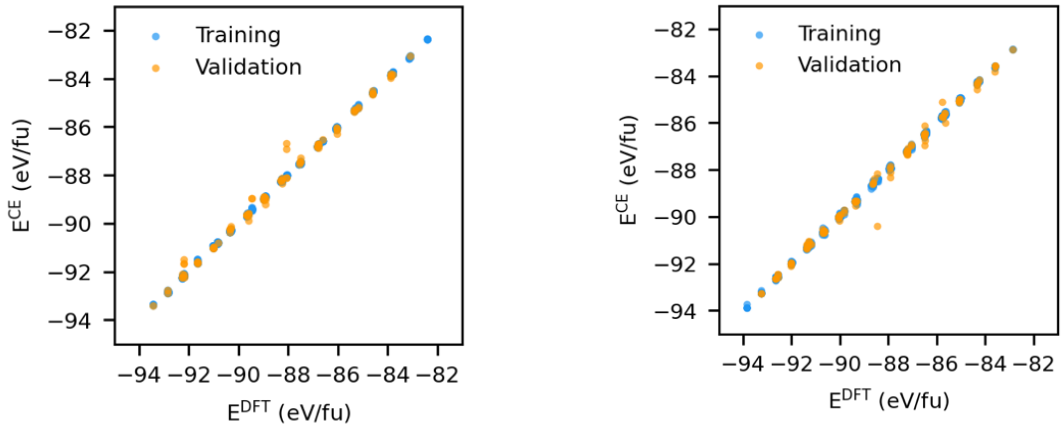

Supplementary Figure 27. Correlation of DFT energies with predicted energies from best cluster expansion models for left) $Li_xFeP_2S_6$ and right) $Li_xFe_{0.75}Mn_{0.25}P_2S_6$

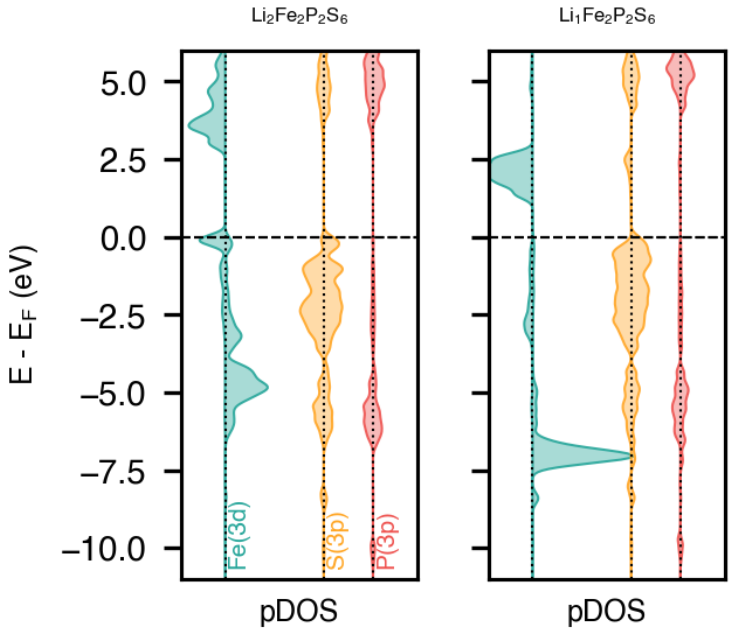

Supplementary Figure 28. Projected density of states of $Li_xFeP_2S_6$ (for x = 2 and 1).

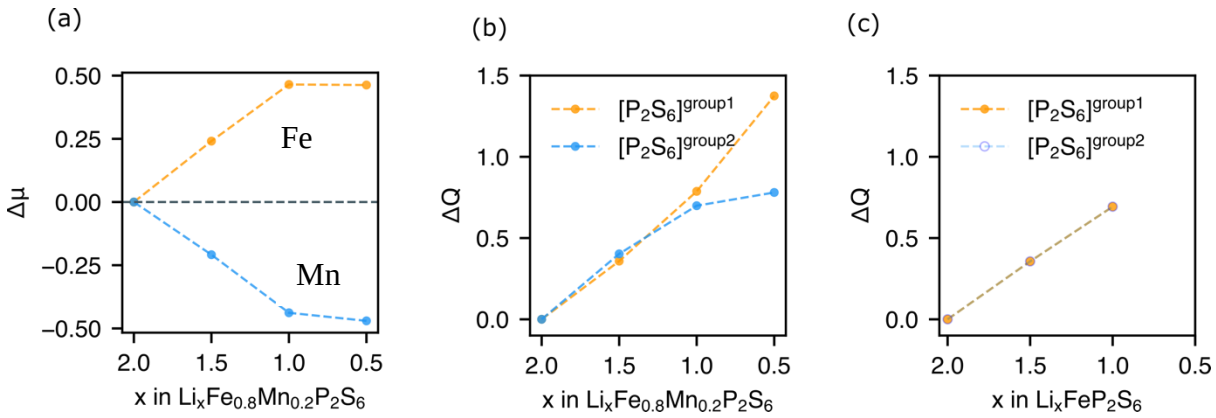

Supplementary Figure 29. (a) changes in the calculated magnetic moments of Fe and Mn in $Li_xFe_{0.0.75}Mn_{0.25}P_2S_6$. The oxidation of Fe increases the number of unpaired electrons, while this is the opposite for Mn oxidation. (b) and (c) changes in the calculated charges of $[P_2S_6]$ units in $Li_xFe_{0.75}Mn_{0.25}P_2S_6$ and $Li_xFeP_2S_6$ (group 1 denotes the $[P_2S_6]$ units that participate in the polyanion redox in $Li_xFe_{0.75}Mn_{0.25}P_2S_6$, and group 2 denotes the non-participating units.) In the $Li_xFe_{0.75}Mn_{0.25}P_2S_6$, polyanion redox is evidenced by increased charges beyond the conventional transition-metal redox limit ($x < 1$).

References

1. Okhotnikov, K., Charpentier, T. & Cadars, S. Supercell program: a combinatorial structure-generation approach for the local-level modeling of atomic substitutions and partial occupancies in crystals. *J. Cheminformatics* **8**, 17 (2016).
2. Xie, T. & Grossman, J. C. Crystal Graph Convolutional Neural Networks for an Accurate and Interpretable Prediction of Material Properties. *Phys. Rev. Lett.* **120**, 145301 (2018).
3. Zarabadi-Poor, P. pzarabadip/aiida-catmat: (2022) doi:10.5281/zenodo.6877599.
4. Sourisseau, C., Forgerit, J. P. & Mathey, Y. Vibrational study of the [$P_2S_4^{-6}$] anion, of some MPS_3 layered compounds (M = Fe, Co, Ni, In_{23}), and of their intercalates with [$Co(\eta^5\text{-}C_5H_5)^{+2}$] cations. *J. Solid State Chem.* **49**, 134–149 (1983).
5. Zhou, Y. *et al.* Observation of Interfacial Degradation of Li_6PS_5Cl against Lithium Metal and $LiCoO_2$ via In Situ Electrochemical Raman Microscopy. *Batter. Supercaps* **3**, 647–652 (2020).
6. Evenson & Dorhout, P. K. Thiophosphate Phase Diagrams Developed in Conjunction with the Synthesis of the New Compounds $KLaP_2S_6$, $K_2La(P_2S_6)_{1/2}(PS_4)$, $K_3La(PS_4)_2$, $K_4La_{0.67}(PS_4)_2$, $K_{9-x}La_{1+x/3}(PS_4)_4$ (x = 0.5), $K_4Eu(PS_4)_2$, and $KEuPS_4$. *Inorg. Chem.* **40**, 2884–2891 (2001).
7. Vysochanskii, Yu. M., Stephanovich, V. A., Molnar, A. A., Cajipe, V. B. & Bourdon, X. Raman spectroscopy study of the ferrielectric-paraelectric transition in layered $CuInP_2S_6$. *Phys. Rev. B* **58**, 9119–9124 (1998).
8. Schoop, L. M. *et al.* Synthesis and Characterization of Three New Lithium-Scandium Hexathiohypodiphosphates: $Li_{4-3x}Sc_xP_2S_6$ (x = 0.358), *m*-$LiScP_2S_6$, and *t*-$LiScP_2S_6$. *Z. Für Anorg. Allg. Chem.* **644**, 1854–1862 (2018).
9. Morgan, B. J. bsym: A basic symmetry module. *J. Open Source Softw.* **2**, 370 (2017).

10. Ångqvist, M. *et al.* ICET – A Python Library for Constructing and Sampling Alloy Cluster Expansions. *Adv. Theory Simul.* **2**, 1900015 (2019).

11. Schwietert, T. K. *et al.* Clarifying the relationship between redox activity and electrochemical stability in solid electrolytes. *Nat. Mater.* **19**, 428–435 (2020).

12. Tan, D. H. S. *et al.* Elucidating Reversible Electrochemical Redox of Li_6PS_5Cl Solid Electrolyte. *ACS Energy Lett.* **4**, 2418–2427 (2019).

13. Auvergniot, J. *et al.* Redox activity of argyrodite Li_6PS_5Cl electrolyte in all-solid-state Li-ion battery: An XPS study. *Solid State Ion.* **300**, 78–85 (2017).